THE ASTROPHYSICAL JOURNAL, 307:575–592, 1986 August 15

RELATIVISTIC STELLAR DYNAMICS ON THE COMPUTER. IV. COLLAPSE OF A STAR CLUSTER TO A BLACK HOLE

STUART L. SHAPIRO[1] AND SAUL A. TEUKOLSKY[1]
Center for Radiophysics and Space Research, Cornell University
Received 1985 October 1; accepted 1986 February 6

ABSTRACT

What is the fate of an unstable star cluster with a highly relativistic core and an extensive Newtonian halo? The answer to this question may throw light on the origin of supermassive black holes in quasars and AGNs, and hence is astrophysically important. From a computational standpoint, however, ascertaining the answer poses a formidable challenge. It calls for the combined machinery of numerical relativity and N-body particle simulations. We solve the problem in this paper.

The collapse of an extreme core-halo cluster leads to the formation of a black hole. The value of the black hole mass is the most significant physical result of our study. Determining this value is numerically difficult because of the large dynamic range that characterizes such a cluster. After the initial implosion, one must allow enough time to elapse so that the configuration can settle down to a stationary state. The new dynamical equilibrium state consists of a central black hole embedded in a stable, extended cluster. The spacetime must be evolved to a stationary state *before* the appearance of numerical or physical singularities associated with black hole formation. We show how, by making an appropriate choice of space and time coordinates and by working with dynamical variables that "freeze" at late times near the center, the complete evolution of such a cluster can be determined. We find that even for very centrally condensed configurations an appreciable fraction of the total cluster mass—much larger than the initial core mass—ultimately collapses to a black hole.

Several coordinate systems have recently been proposed for doing numerical relativity. We have compared these in detail during our simulations of the collapse of very extreme configurations of collisionless matter. These comparisons, made in spherical symmetry, yield insights for future multidimensional work.

Subject headings: black holes — clusters: globular — relativity

I. INTRODUCTION

It is now possible to integrate the full Einstein equations for the dynamical motion of an arbitrary, spherical, *collisionless* configuration in general relativity (Shapiro and Teukolsky 1985*a*, *b*, *c*; hereafter Papers I, II, and III, respectively). One can follow on the computer the dynamical evolution of a relativistic star cluster by combining the techniques of numerical relativity with those of N-body particle simulations. The resulting scheme is even able to handle epochs characterized by total gravitational collapse leading to the formation of a black hole. These general relativistic Vlasov integrations follow the formation and growth of the black hole accurately without the appearance of numerical or physical singularities.

In Paper I we presented some historical background to this problem, together with a detailed discussion of the computational method and a battery of test-bed calculations that help assess the reliability of our code. In Paper II we applied the code to address several long-standing theoretical issues in relativistic stellar dynamics, including the stability of relativistic star clusters in dynamical equilibrium, the collapse of unstable star clusters to black holes, and relativistic "violent relaxation." Based on our findings, we proposed in Paper III a plausible scenario for the origin of quasars and AGNs via the collapse of dense star clusters embedded in galactic nuclei to supermassive black holes.

We attempted to show in these papers that "relativistic stellar dynamics on the computer" was an endeavor ripe for computational and astrophysical exploration. Probing this area provides fresh insights into nonlinear dynamics and general relativity. It establishes a new laboratory in which to test numerical algorithms for the construction of spacetimes. It also opens up some promising avenues for the formation of supermassive black holes in nature which are believed to be the likely sources of energy in quasars and AGNs (see reviews by Begelman, Blandford, and Rees 1984; Rees 1984, and references therein).

In spite of our successes in solving the spherical stellar dynamics problem in general relativity, our previous work had some notable limitations. Specifically, some of our integrations of collapsing clusters had to terminate well before the exterior spacetimes surrounding a growing, central black hole reached a final stationary state. Thus it was not always possible for us to determine exactly what fraction of the total mass of the cluster ultimately forms a black hole and what fraction remains outside in orbit about the central hole. Not surprisingly, this problem was most severe when we evolved clusters with appreciable *central concentration*. Such configurations by construction are characterized by enormous dynamic range, with the dynamical (orbit) time scale in the central core significantly shorter than the dynamical time scale in the outer halo. Following the orbits of the central stars near the event horizon accurately on time scales sufficiently long to track the outer halo stars is crucial for determining the final fate of the configuration. This requirement imposed the ultimate limitation on the ability of our code to integrate arbitrarily far into the future.

[1] Departments of Astronomy and Physics, Cornell University, Ithaca, NY 14853.

Overcoming the above limitation is not merely of pedagogic interest. For as we demonstrated in Paper III, *if relativistic star clusters do form in nature, they are likely to be very centrally condensed.* Moreover, *the most interesting astrophysical scenarios—those that may be relevant to the birth of quasars and AGNs—involve the catastrophic collapse of extreme core-halo configurations with relativistic cores and extensive Newtonian halos.* These are precisely the clusters for which one would like to determine the final size of the black hole, but for which our previous integrations had to terminate well before the evolution was completed.

Equally relevant, numerical problems encountered in evolving extreme core-halo *spherical* clusters often resemble problems that arise when trying to follow the propagation of gravitational waves during the evolution of *nonspherical* systems in general relativity. In the latter situation, one must follow accurately the motion of matter near a black hole event horizon whole simultaneously tracking the propagation of any radiation out to much larger radii. The complexity of this problem is also due, in part, to the vast dynamic range that characterizes a spacetime with a localized region of strong gravitational fields as well as outgoing gravitational waves. Experience gained in solving the centrally condensed, spherical cluster problem may thus prove useful in the construction of reliable 2 + 1 and 3 + 1 dimensional numerical codes that can handle strong-field spacetimes with gravitational radiation.

One cause of our inability to track the late evolution of highly condensed clusters was our overly conservative choice of an integration *time-step criterion* (eq. [62] in Paper I). Recognizing the role of the lapse function α in holding back the evolution in the central regions readily enables us to revise this criterion and speed up the integrations considerably, as we discuss below.

Two other causes are more troublesome to deal with. They arise from our adopted choices of a time-slicing condition and radial coordinate: *maximal* time slicing and *isotropic* radial coordinates. These choices were made to prevent the appearance of singularities associated with black hole formation during the evolution. The ability to choose such coordinates, if they exist, is a gauge freedom inherent in general relativity. One can easily take advantage of this freedom in the 3 + 1 Arnowitt-Deser-Misner (ADM) formulation of Einstein's equations, which we employ to determine the metric field quantities. (For an extensive discussion of the ADM approach and a comparison of some potentially useful gauge choices for numerical work, see articles in Smarr 1979 and Deruelle and Piran 1983, and references therein.) Unfortunately, isotropic coordinates, while preventing "spikes" from forming in the radial metric component (Smarr and York 1978), lead to considerable *grid stretching* all along the black hole throat (see Fig. 1). Grid stretching occurs because the isotropic radial coordinate r is forced to span many decades along the black hole throat. The metric field also varies rapidly on the throat. As a consequence, it is necessary to cover the throat with a growing number of grid points to determine the metric accurately in a numerical calculation. However, with the computational limitation of only a finite number of radial grid points available to cover the throat, the growing numerical inaccuracies induced by grid stretching ultimately force the integrations to terminate. Furthermore, maximal time slicing, while successful in holding back the advance of proper time at the center and thus postponing the formation of singularities, causes the lapse function α to decay and the spatial conformal factor A to increase exponentially rapidly at late times at the center. Thus underflows and overflows in the metric components may eventually accompany black hole formation, terminating the integrations before the exterior spacetime reaches a final stationary state.

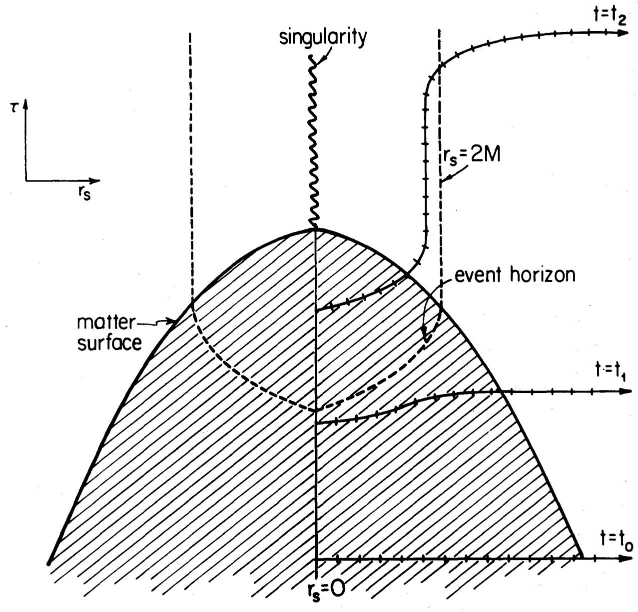

FIG. 1.—Schematic spacetime diagram of the collapse of a star cluster to a black hole. Vertical axis is the proper time τ of particle world lines, and horizontal axis is areal (Schwarzschild) coordinate r_S. Singularity forms at the center in a finite proper time. In a numerical calculation one chooses a time slicing t that does not encounter the singularity by slowing down the advance of proper time near the center. Shown are three time slices during the collapse. Tick marks on each slice represent a radial grid based on the isotropic coordinate r. When the spatial metric on the time slice t has the "radial" form $A_S^2 dr_S^2 + r_S^2 d\Omega^2$, a spike develops in A_S near the event horizon, as in the usual static Schwarzschild geometry, even though no *physical* singularity is encountered. When the isotropic spatial metric $A^2dr^2 + A^2r^2d\Omega^2$ is used, no spike appears. However, considerable radial grid must be expended along the throat near the horizon in order to determine the metric there accurately.

The unsatisfactory situation described above compels us to search for a better choice of spacetime coordinates to solve the problem of centrally condensed spherical clusters. The "great goal" of numerical relativity has always been to construct a code which (1) avoids singularities, (2) maintains high accuracy, and (3) can run forever. Only by successfully resolving the computational difficulties posed by centrally condensed clusters will we have confidence that this goal can be realized in practice.

In this paper we tackle the above problem head-on. Specifically, we systematically implement improvements to the "standard" numerical scheme described in Paper I that make it more useful for handling extreme core-halo configurations. These improvements range from minor adjustments of the basic algorithms (e.g., altering the time-step criterion) to major revisions of the code based on a new set of dynamical equations. For example, we consider an alternative time coordinate based on *polar* time slicing. Since *no apparent horizon* can form on polar hypersurfaces during spherical collapse, there is the suspicion that this time-slicing condition possesses stronger singularity avoidance features than maximal time slicing (Piran 1983) and is thus advantageous for solving the condensed cluster problem. This motivates a detailed comparison of the numerical spacetimes generated by collapsing clusters in the two time gauges. We consider a further revision by exploiting the desirable feature that in either gauge the advance of proper time slows down at the center as coordinate time increases. This feature enables us to recast the equations in such a way that some of the fundamental dynamical variables (e.g., the particle radii and velocities) explicitly "freeze" at late times at the center. Rewriting the equations in terms of these frozen variables yields an efficient scheme that indeed "runs forever." This scheme appears to be the optimal way to determine the final fate of extreme core-halo clusters that undergo catastrophic collapse to black holes.

The key astrophysical result of this paper is that we are able to follow the collapse of an unstable relativistic star cluster with an extensive, Newtonian halo sufficiently far in time to observe that (1) a substantial black hole forms at the cluster center, (2) the hole typically contains a significant fraction of the total cluster mass—many times the original core mass—but most of the cluster remains far outside in orbit about the hole, and (3) the system ultimately settles down to a new, dynamically stable equilibrium state consisting of a massive black hole embedded in a quasi-Newtonian star cluster. This final configuration may provide the basis for understanding quasars and AGNs. Our computations thus demonstrate a possible route by which such a configuration may actually arise in nature.

The key computational consequence of this paper is that we are able to explore via concrete examples the relative merits of several different coordinate choices currently favored for doing numerical relativity. Devoid of the numerical complications that inevitably arise from shocks and other hydrodynamic discontinuities, our Vlasov simulations may furnish the cleanest laboratory yet for performing comparative studies of this kind. Such studies are most valuable in preparation for work in higher dimensions, where disentangling physically real from pure gauge (i.e. coordinate) effects becomes even more complicated.

In § II we present the key new equations that we employ in revised versions of our basic numerical scheme. In § III we briefly sketch how these equations may be assembled in different combinations to yield several computationally distinct versions of the code. In this section we also present the results of some crucial test-bed calculations that judge the absolute and relative reliability of these various versions. In § IV we summarize our new numerical results. In § V we discuss the astrophysical and numerical significance of our findings. Here we also provide a rough analytic estimate that confirms our numerical calculation of the mass fraction that ultimately forms a supermassive black hole in an extreme core-halo cluster that undergoes gravitational collapse.

II. BASIC EQUATIONS

a) *Polar Slicing*

We again adopt the isotropic form of the metric, as in equation (I.1):[2]

$$ds^2 = -(\alpha^2 - A^2\beta^2)dt^2 + 2A^2\beta dr dt + A^2(dr^2 + r^2 d\theta^2 + r^2 \sin^2\theta d\phi^2) . \quad (1)$$

As discussed in Paper I, one of the challenges of numerical relativity is to find a good choice of coordinates so that one can actually solve the problem posed without encountering singularities. The previous papers in this series used a time coordinate defined by the *maximal slicing* condition. Mathematically, maximal slicing is defined by setting the trace of the extrinsic curvature of the t = constant slices to zero:

$$\mathrm{Tr}\, K_{ij} \equiv K_i^i = 0 . \quad (2)$$

Taking the trace of the evolution equation for $\partial_t K_{ij}$ then leads to an elliptic equation (eq. [I.15]) for the lapse function α. In spherical symmetry, with the metric (1), the equation reduces to equation (I.31).

A different time-slicing condition has been proposed by Eardley (1982) and by Bardeen and Piran (1983). This is the *polar slicing* condition: set the trace of the *transverse* part of K_{ij} to zero, that is, the part orthogonal to the radial direction. This can be written

$$K_{\mathrm{T}} \equiv K_\theta^\theta + K_\phi^\phi = 0 . \quad (3)$$

The primary motivation for polar slicing was to find a coordinate condition that would make it easier to compute the amount of gravitational radiation emitted in nonspherical gravitational collapse. It was also hoped that this condition might have better singularity avoidance than maximal slicing when a black hole forms. This hope arises because polar slicing avoids regions of spacetime containing trapped surfaces in spherical symmetry, and trapped surfaces signal the presence of an event horizon and the impending formation of a singularity.

In polar slicing, the matter equations are unchanged from their form in maximal slicing, namely equations (I.2)–(I.11). The equations for the metric variables are, however, different.[3] It is convenient to use the quantity K_{T} to write equations valid in either gauge:

$$K_{\mathrm{T}} = \begin{cases} 0 , & \text{polar slicing ,} \\ -K_r^r , & \text{maximal slicing .} \end{cases} \quad (4)$$

Then the evolution equation for the metric coefficient A is

$$A_{,t} = \beta\left(A_{,r} + \frac{A}{r}\right) - \frac{1}{2}\alpha A K_{\mathrm{T}} . \quad (5)$$

Here the comma denotes a partial derivative. The Hamiltonian constraint becomes

$$\frac{1}{r^2}\frac{\partial}{\partial r}\left(r^2 \frac{\partial}{\partial r} A^{1/2}\right) = -\frac{A^{5/2}}{4}\left(8\pi\rho + \frac{3K_{\mathrm{T}}^2}{4}\right) . \quad (6)$$

The shift β is given by the equation

$$\beta = -r\int_r^\infty \alpha\left(K_r^r - \frac{1}{2}K_{\mathrm{T}}\right)\frac{dr}{r} . \quad (7)$$

The momentum constraint determines the radial component of the extrinsic curvature:

$$K_r^r = \begin{cases} -\dfrac{8\pi}{A^3 r^3}\displaystyle\int_0^r A^3 r^3 t_r\, dr , & \text{maximal,} \\ -\dfrac{4\pi r t_r}{1 + rA_{,r}/A} , & \text{polar .} \end{cases} \quad (8)$$

[2] Here and throughout the paper, the prefix "I" refers to equations from Paper I, and similarly for "II."

[3] The equations we derive here do not agree with the spherical limit of the equations in Appendix B of Bardeen and Piran (1983), which contain errors.

The lapse equation, equation (I.31) for maximal slicing, is replaced in polar slicing by

$$\alpha = \frac{A_{\max}\alpha_{\max}}{A}\exp\left[\frac{1}{2}\int_{r_{\max}}^{r}\frac{r(A_{,r}/A)^2 + 8\pi r S_{rr}}{1 + rA_{,r}/A}\,dr\right]. \tag{9}$$

Here the source term S_{rr} is defined by the radial component of the stress-energy tensor:

$$S_{rr} = T_{rr} = \sum_A m_A n_A u_{r(A)} u_{r(A)} \tag{10}$$

(notation as § III*d* of Paper I). Equation (9) is derived from the condition that polar slicing hold throughout the evolution,

$$\frac{dK_{\rm T}}{dt} \equiv \left(\frac{\partial}{\partial t} - \beta^i \frac{\partial}{\partial x^i}\right)K_{\rm T} = 0\,, \tag{11}$$

together with equations (6) and (I.32). Note that the source term S_{rr} replaces the quantity T defined in equation (I.46), which is no longer needed in polar slicing.

The boundary conditions on the metric variables are very simple in polar slicing, because the metric must reduce to the isotropic form of the Schwarzschild metric as $r \to \infty$. We can in fact show that the metric takes the isotropic Schwarzschild form *everywhere* outside the matter: set the right-hand side of equation (6) to zero and integrate. Require that A tend asymptotically to the isotropic Schwarzschild value at large r, and hence find that

$$A = \left(1 + \frac{M}{2r}\right)^2 \tag{12}$$

for all r outside the matter. Substitute this result in equation (9), with $S_{rr} = 0$, and get

$$\alpha = \frac{1 - M/(2r)}{1 + M/(2r)}\,, \tag{13}$$

which is the usual isotropic Schwarzschild value. Equation (8) shows that $K_r^r = 0$ everywhere outside the matter, and hence by equation (7) $\beta = 0$, too. Thus in polar slicing one need only integrate Einstein's equations *inside* the matter, with Schwarzschild boundary conditions imposed at the matter surface. This is in contrast to maximal slicing, where the nonzero β and K_r^r require the metric to be integrated to reasonably large values of r in the vacuum exterior.

Polar slicing also entails some changes in the diagnostics available to monitor the accuracy of the numerical computation. Equation (I.47) for the total mass M in the exterior is trivially satisfied because we are imposing the exact Schwarzschild solution in the exterior. The check therefore reduces to seeing whether the expression for M formed from the gradient of A is continuous at the surface.

The trapped surface condition (I.53) can be written more generally as

$$1 + rA_{,r}/A - \tfrac{1}{2}rAK_{\rm T} \le 0\,, \tag{14}$$

with equality holding at the apparent horizon, the outer boundary of the region of trapped surfaces. In polar slicing, $K_{\rm T} = 0$. Thus the existence of trapped surfaces in polar slicing would be equivalent to the condition

$$\frac{dr_{\rm S}}{dr} \le 0\,, \tag{15}$$

where

$$r_{\rm S} = Ar \tag{16}$$

is the Schwarzschild areal radial coordinate. In a nonpathological spacetime $r_{\rm S}$ is a monotonic increasing function as one moves outward to larger r, and hence no trapped surfaces are encountered in polar slicing. Trapped surfaces are generally found in the maximal slicing of the same spacetime, but the polar slices avoid those regions.

Determining the velocity profiles of the particles is often useful. Alternative recipes for doing this are summarized in Appendix A.

b) α Freezing

Recall the physical meaning of the lapse function α: it gives the lapse of proper time $d\tau$ measured by an observer at rest in the t = constant hypersurfaces, for a given lapse of coordinate time dt,

$$d\tau = \alpha dt\,. \tag{17}$$

Such an observer is called a *normal* observer because his world line is orthogonal to the t = constant hypersurface.

At late times during gravitational collapse, the lapse goes to zero exponentially with t near the center of the configuration (the "collapse of the lapse"; see Paper I for discussion). We therefore expect quantities measured by the normal observer there to *freeze*, or become constant with t at late times, because there is no lapse of proper time in the normal observer's reference frame.

As an example, consider the radial component of the velocity of a particle, $v^{\hat r}$, where the caret denotes a component measured by the normal observer. We have

$$v^{\hat r} = \frac{u^{\hat r}}{u^{\hat 0}} = -\frac{\boldsymbol{u}\cdot\boldsymbol{e}_{\hat r}}{\boldsymbol{u}\cdot\boldsymbol{e}_{\hat 0}}\,. \tag{18}$$

The time basis vector $\boldsymbol{e}_{\hat 0}$ is just the 4-velocity of the normal observer, which is the unit normal $\boldsymbol{n}$ with components given by equation (I.18). The radial basis vector is related to the coordinate radial basis vector by $\boldsymbol{e}_{\hat r} = \boldsymbol{e}_r/A$. Thus equation (18) becomes

$$v^{\hat r} = \frac{u_r/A}{\alpha u^0}\,. \tag{19}$$

Similarly

$$v^{\hat\phi} = \frac{u_\phi/Ar}{\alpha u^0}\,. \tag{20}$$

Substituting equations (19) and (20) in equation (I.11) gives

$$\alpha u^0 = \frac{1}{[1 - (v^{\hat r})^2 - (v^{\hat\phi})^2]^{1/2}}\,. \tag{21}$$

Since $v^{\hat r}$ and $v^{\hat\phi}$ must freeze at late times, so must αu^0, and since u_ϕ is a constant of the motion, we see from equations (19) and (20) that the *areal* radius of a particle $r_{\rm S} \equiv Ar$ and the quantity u_r/A also freeze.

Other quantities that freeze at late times in regions where $\alpha \to 0$ are related to the proper 3-volume comoving with a particle, $\mathscr{V}_A$, where subscript A is the particle label:

$$\mathscr{V}_A = 4\pi\int_{r_{i-1/2}}^{r_{i+1/2}}(\alpha u_0)_A A^3 r^2 dr\,. \tag{22}$$

Suppose we choose radial zones that are bounded by radial coordinates r_i corresponding to *fixed* areal radius $r_{\rm S}$. Then at late times t, since the particle positions $r_{\rm S}$ are frozen wherever

$\alpha \to 0$, the particle *number* in such zones freezes too. We can also see that $\mathscr{V}_A$ is frozen. Using equation (16), we rewrite equation (22) as

$$\mathscr{V}_A = 4\pi \int_{r(r_{S_1})}^{r(r_{S_2})} (\alpha u_0)_A r_S^2 A dr , \tag{23}$$

where r_{S_1} and r_{S_2} are constant with t. But from equation (1) we see that Adr is just the proper radial distance measured by the normal observer, and so it freezes. (A formal proof of this point is given in Appendix B.) Hence $\mathscr{V}_A$ freezes too.

Equations (I.43) and (I.46) now show us that as functions of r_S the source profiles ρ and T freeze whenever $\alpha \to 0$. Note that the source profiles t_r and S_{rr} do *not* freeze since they depend on u_r, not u_r/A. Similarly, while equations (8), (26), and (I.45) show that K_r^r *does* freeze when evaluated at constant r_S, the quantities β, A, and r (*isotropic* radius of a particle) do not. For example, equation (I.8) shows explicitly that even when $\alpha \to 0$, the shift β continues to drive changes in r.

When α becomes small at late times near the center of a collapsing configuration, it is customary in numerical work not to allow it to fall below some small value $\alpha_{\min}$ to avoid underflows. Since some quantities in the numerical evolution do get large, the question arises of exactly how small a value of $\alpha_{\min}$ is required. Having identified the variables that freeze, we note that cutting off α at $\alpha_{\min} \ll 1$ is entirely justified for equations involving those variables, but could be risky for variables that do not freeze.

c) *Equations in Asymptotically Freezing Variables*

For practical implementation we need the actual form of the equations using the variables that freeze. In either time slicing, the equation of motion of a particle becomes

$$\frac{dr_S}{dt} = \frac{\partial(Ar)}{\partial t} + \frac{dr}{dt}\frac{\partial(Ar)}{\partial r}$$
$$= -\frac{1}{2}\alpha r_S K_T + \alpha \frac{u_r/A}{\alpha u^0}\left(1 + \frac{r_S A_{,r}}{A^2}\right), \tag{24}$$

where we have used equations (5) and (I.8). Now equation (16) gives

$$\frac{\partial}{\partial r} = \frac{1}{\partial r/\partial r_S}\frac{\partial}{\partial r_S} = \frac{A}{1 - r_S A_{,r_S}/A}\frac{\partial}{\partial r_S}, \tag{25}$$

and so

$$1 + \frac{r_S A_{,r}}{A^2} = 1\bigg/\left(1 - \frac{r_S A_{,r_S}}{A}\right). \tag{26}$$

Thus an alternative form of equation (24) is

$$\frac{dr_S}{dt} = -\frac{1}{2}\alpha r_S K_T + \alpha \frac{u_r/A}{\alpha u^0}\bigg/\left(1 - \frac{r_S A_{,r_S}}{A}\right). \tag{27}$$

Similarly equation (I.9) becomes

$$\frac{d}{dt}\left(\frac{u_r}{A}\right) = -\frac{(\alpha u^0)\alpha_{,r}}{A} + \alpha\left(1 + \frac{r_S A_{,r}}{A^2}\right)\frac{u_\phi^2}{r_S^3(\alpha u^0)}$$
$$+ \alpha K_r^r\left(\frac{u_r}{A}\right) \tag{28}$$
$$= \left[-(\alpha u^0)\alpha_{,r_S} + \alpha\frac{u_\phi^2}{r_S^3(\alpha u^0)}\right]\left(1 - \frac{r_S A_{,r_S}}{A}\right)^{-1}$$
$$+ \alpha K_r^r\left(\frac{u_r}{A}\right). \tag{29}$$

To get equation (28) we have used equations (5) and (7) to eliminate $A_{,t}$ and $\beta_{,r}$ respectively. The alternative form (29) is obtained using equation (26).

Since every term on the right-hand sides of equations (24) and (28) contains an explicit α or $\alpha_{,r}$, we see that

$$\frac{dr_S}{dt} \to 0\,, \quad \frac{d}{dt}\left(\frac{u_r}{A}\right) \to 0 \quad \text{as } \alpha \to 0\,. \tag{30}$$

This is a formal demonstration of the freezing of the particle motion at late times near the center of a collapsing configuration in maximal or polar slicing.

Besides the equations of motion, we need the appropriate equations for the metric variables. Consider equation (5). We have

$$\left.\frac{\partial A}{\partial t}\right|_{r_S} = \left.\frac{\partial A}{\partial t}\right|_r + \left.\frac{\partial r}{\partial t}\right|_{r_S}\left.\frac{\partial A}{\partial r}\right|_t. \tag{31}$$

But equation (16) gives

$$\left.\frac{\partial r}{\partial t}\right|_{r_S} = -\frac{r_S^2}{A^2}\left.\frac{\partial A}{\partial t}\right|_{r_S}, \tag{32}$$

and so equation (5) becomes

$$\left.\frac{\partial A}{\partial t}\right|_{r_S} = \frac{A^2\beta}{r_S} - \frac{1}{2}\alpha A K_T\left(1 - \frac{r_S A_{,r_S}}{A}\right). \tag{33}$$

Here we have used equation (26) to obtain the final result.

Equation (9) for the lapse in polar slicing can be transformed by the change of variable $dr \to (dr/dr_S)dr_S$. Using equations (16) and (26), we find

$$\alpha = \frac{A_{\max}\alpha_{\max}}{A}\exp\left\{\frac{1}{2}\int_{r_{S,\max}}^{r_S}\left[r_S\left(\frac{A_{,r_S}}{A}\right)^2 + \frac{8\pi r_S S_{rr}}{A^2}\left(1 - \frac{r_S A_{,r_S}}{A}\right)^2\right]dr_S\right\}. \tag{34}$$

Equation (I.31) for the lapse in maximal slicing can be similarly transformed to yield

$$\frac{\partial}{\partial r_S}\left(\frac{r_S^2}{1 - r_S A_{,r_S}/A}\frac{\partial\alpha}{\partial r_S}\right)$$
$$= \alpha r_S^2\left(1 - \frac{r_S A_{,r_S}}{A}\right)\left(\frac{3}{2}K_T^2 + 8\pi\rho + 4\pi T\right). \tag{35}$$

Similarly one can transform equation (7) for β and equation (8) for K_r^r to equations involving r_S.

Note that when using r_S as the grid coordinate, one must transform the volume element used in source terms such as ρ, t_r, and S_{rr}. Equation (23) becomes

$$\mathscr{V}_A = 4\pi\int_{r_{S_1}}^{r_{S_2}}(\alpha u_0)_A r_S^2 A\frac{dr}{dr_S}dr_S$$
$$= 4\pi\int_{r_{S_1}}^{r_{S_2}}(\alpha u_0)_A r_S^2\left(1 - \frac{r_S A_{,r_S}}{A}\right)dr_S\,, \tag{36}$$

where we have used equation (16). This equation is used instead of equation (22) in the source terms (see eq. [I.44]).

III. ALTERNATIVE COMPUTATIONAL STRATEGIES

a) *Assembling the Equations*

In this section we sketch different ways that the fundamental equations can be assembled to yield several computationally distinct versions of the basic code. The original version based on maximal time slicing and isotropic coordinates was already detailed in Paper I. The one significant change we have incorporated into this scheme was to revise the time-step criterion to account for the slowing down of *proper* time with respect to *coordinate* time as the lapse function α falls to zero. Thus in place of equation (I.62) we now substitute

$$\Delta t = \frac{q}{\alpha}\left(\frac{3\pi}{32\rho_{\max}}\right)^{1/2}, \quad \rho_{\max} = \max\{\rho_i\}, \quad 1 \le i \le N_f. \quad (37)$$

The insertion of α in the denominator makes the integration scheme considerably more efficient. We can take a much bigger step in coordinate time before updating the gravitational metric field quantities (see Paper I, especially Fig. 1, for a review of the logical flow). Equation (37) still guarantees that the matter source terms for these field quantities change only a small amount between time steps, because they change only when proper time as measured by a normal observer (eq. [17]) increases by a significant fraction of the local free-fall time.

Polar time slicing yields another version of this code. The necessary equations were presented in § II*a*. A brief sketch of this code's logical flow is given in Figure 2. Both the original maximal and the new polar versions are based exclusively on isotropic radial coordinates. Together they constitute what we shall refer to as the *standard* code. The standard code has the virtue that the metric is everywhere a smooth function of the isotropic radial coordinate r, even when a black hole forms. Thus there are no "spikes" in the metric near the horizon as in the case of the so-called "radial" metric based on the areal coordinate r_S (see Petrich, Shapiro, and Teukolsky 1986 for a demonstration in the case of Oppenheimer-Snyder collapse). Such spikes inevitably result in numerical inaccuracies, particularly in regions of greatest interest near a black hole. However, employing isotropic coordinates has the limitation that considerable grid stretching eventually develops along the throat of a black hole (see Fig. 1). Thus, smoothness of the metric near a black hole is preserved at late times only by inserting many grid points there.

Some of the above difficulties are circumvented by rewriting the fundamental equations in terms of new variables, as described in § II*b* above. Thus, the particle variables r and u_r are replaced by r_S and u_r/A, respectively. These variables have the virtue that they freeze at late times wherever α becomes small, thereby reducing the orbit integration time and resulting

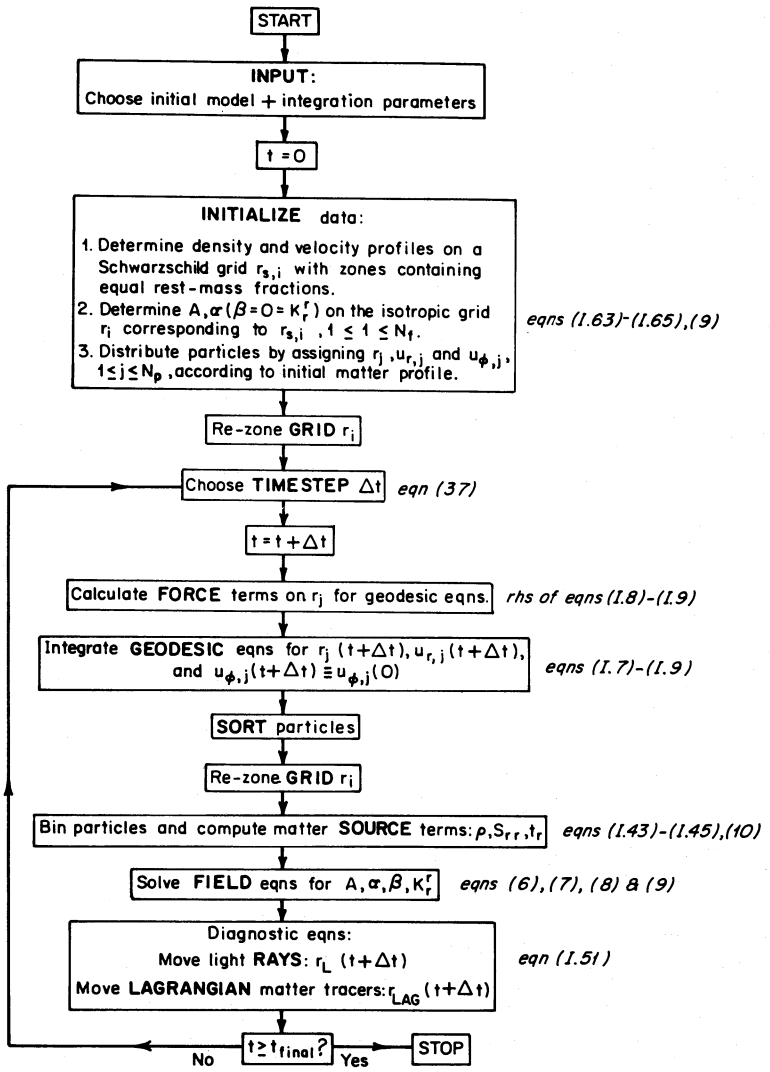

FIG. 2.—Logical flowchart of the numerical method for implementing the standard version in polar slicing

TABLE 1

ALTERNATIVE SCHEMES COMPARED

Parameter	Standard	Freezing	Hybrid
Time slicing	Maximal or polar	Maximal or polar	Maximal or polar
Particle coordinates	r, u_r, u_ϕ	r_S, u_r/A, u_ϕ	r_S, u_r/A, u_ϕ
Grid coordinate for binning source terms	r	r_S	r_S
A solver	(i) Guess via evolution eq. (5) (ii) Refine via Hamiltonian constraint eq. (6)	Evolution eq. (33)	(i) Guess via evolution eq. (33) (ii) Transform from r_S to $r = r_S/A$ (iii) Refine via Hamiltonian constraint eq. (6)
α solver	Lapse eq. (I.31) or (9)	Lapse eq. (35) or (34)	(i) Transform from r_S to $r = r_S/A$ (ii) Lapse eq. (I.31) or (9)
Advantages	Metric is a smooth function of r	Asymptotic freezing of particle variables inside black hole; no grid stretching on black hole throat	Asymptotic freezing of particle variables inside black hole; metric solved as a smooth function of r
Disadvantages	Grid stretching on black hole throat	Steep metric gradients on black hole throat	Grid stretching (in r) on black hole throat
Conclusions	Most reliable general purpose scheme	Essential for evolving a collapsing extreme core-halo configuration to a final stationary state	Not much advantage over standard code

integration error for such particles considerably. Once the particles are binned and the matter source terms are computed on the r_S radial grid, the metric field quantities can be determined as functions of r_S. This last step may be accomplished in one of two different ways. We can either rewrite the isotropic field equations in terms of r_S as in § IIc and solve them directly *or* we can (numerically) determine the values of $r = r_S/A(r_S)$ at the r_S grid points and solve the field equations in terms of r as in the standard code. The first method, which involves r_S exclusively, results in the *freezing* version of the code, while the second method, which involves both r and r_S, results in the *hybrid* version. Both of these versions require the use of the evolution equation (33) for A. The solution for A is ultimately refined in the hybrid version by solving the Hamiltonian constraint equation (6) on the isotropic lattice r, exactly as in the standard code (see Paper I). No refinement is performed in the freezing version since rewriting the isotropic Hamiltonian constraint equation in terms of r_S instead of r results in a highly nonlinear elliptic equation which is very difficult to solve accurately.

The distinguishing traits of the three versions of our basic numerical code are compared in Table 1. Note that they are all based on the isotropic line element, even though the areal radius r_S is employed in the freezing and hybrid versions in the calculation of the isotropic metric coefficients. Accordingly, no spikes appear in the metric quantities near a black hole event horizon, although the metric can vary rapidly with r_S in this region at late times. Empirically the different versions require about the same CPU time to evolve a typical spacetime to the same time slice with comparable accuracy.

Our experience indicates that for typical configurations with moderate central concentration the standard code provides the most accurate numerical spacetimes. This is due in part to the greater reliance of the other two versions on the evolution equation for A, which can never be solved as accurately as the elliptic Hamiltonian equation for the same expenditure of computer time. The Hamiltonian equation can be refined to arbitrary accuracy in the standard code without having to transform back and forth between the radial coordinates r and r_S, and this results in greater accuracy. However, for extreme configurations with appreciable central concentrations, highly relativistic cores, and extensive Newtonian halos, the freezing version proves to be essential. An enormous dynamic range is necessary to track the evolution of the more distant particles until their fates have been determined, while continuing to follow the central particles accurately. By freezing the coordinates of those particles that wander near or inside a central black hole, this version of the code is able to cope with this dynamic range. We explore this capability in greater detail in § IV below by means of a concrete example. We have discovered that there seems to be little advantage in employing the hybrid version over one or the other two versions, whichever may be more appropriate for the degree of central concentration in the initial configuration.

b) Test-Bed Calculations: Oppenheimer-Snyder Collapse

In Paper I we presented an intensive and systematic battery of test-bed calculations designed to evaluate the overall performance and reliability of our numerical scheme (see § VI and especially Table 1 of Paper I). All of these tests were performed on the standard version with maximal time-slicing, and the results, which were highly positive, were summarized in that paper. We have performed many of the same tests again in order to assess the relative reliabilities of the three different versions of our basic code and to compare the strengths and weaknesses of the various coordinate systems for handling different sets of initial data.

Foremost among the tests is the dynamical evolution of a homogeneous dust ball, initially at rest. This example provides a stringent test of the ability of our code to follow the collapse of a collisionless system to a black hole. The complete solution is known analytically (Oppenheimer and Synder 1939) and can be expressed in closed form in the familiar Friedmann *comoving, synchronous* coordinate system. In order to evaluate

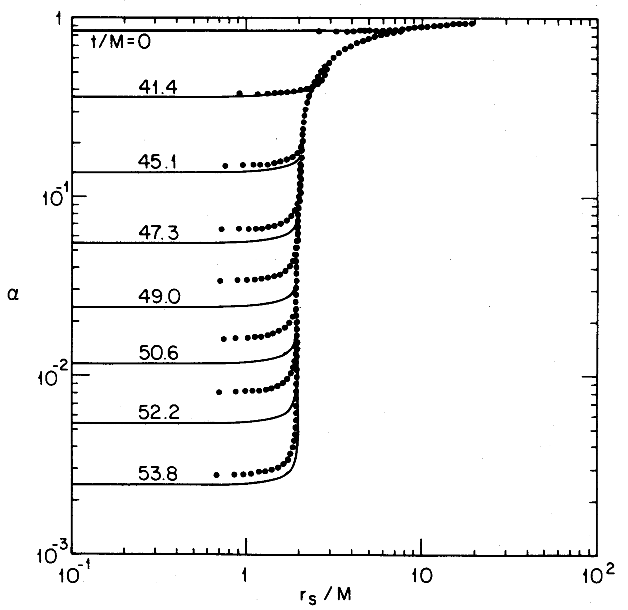

FIG. 3

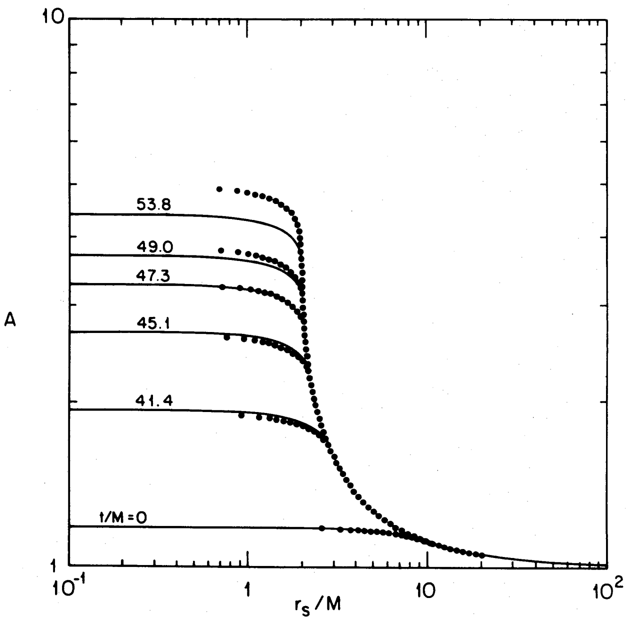

FIG. 4

FIG. 3.—Lapse function α as a function of areal radius r_S on selected polar time slices for Oppenheimer-Snyder collapse from $R = 10\ M$. Solid lines are the results of exact integrations by PST2. Dots are the results obtained with the hybrid code described here. See text for further details.

FIG. 4.—Metric component A as a function of areal radius r_S for the case described in Fig. 3.

the computer generated spacetimes, however, the exact solution must be transformed to the maximal and polar coordinate systems. The necessary numerical transformations and the complete solution for homogeneous dust collapse in both maximal and polar time slicings is presented in Petrich, Shapiro, and Teukolsky (1985) and (1986), respectively (hereafter PST1 and PST2).

In Figures 3–10 we compare the "exact" results of PST2 with the hybrid version of our code in polar time slicing. The case illustrated is for a dust sphere with initial (areal) radius $R/M = 10$ at $t = 0$. The same case was shown in Paper I in maximal time slicing and used there to assess the standard version. Here we adopt a set of integration accuracy parameters similar to the set employed there for generating the numerical spacetime: $N_f = 120$ radial grid points, of which 60 were used to cover the interior with the rest residing in the vacuum exterior; $N_p = 1180$ particles; and time-step parameter $q = 0.0125$, using the "old" time-step criterion, equation (I.62). Note that polar slicing requires many fewer exterior grid points than maximal because the exterior metric is known

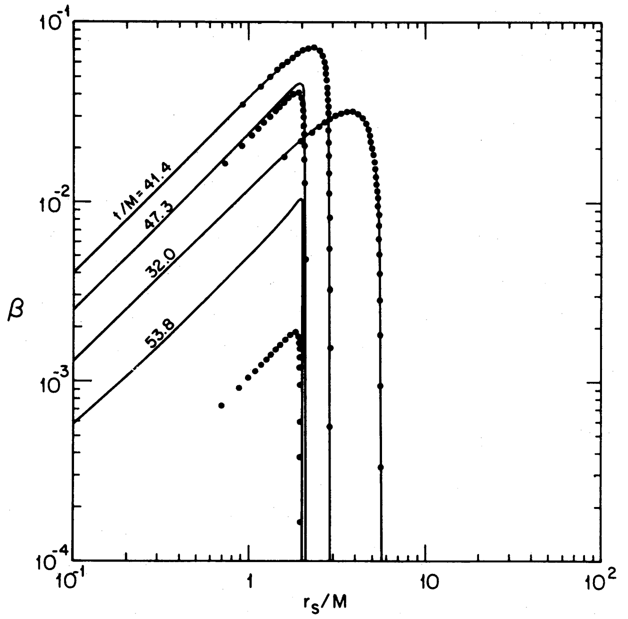

FIG. 5.—Metric component β as a function of areal radius r_S for the case described in Fig. 3. At $t = 0$, $\beta = 0$ everywhere.

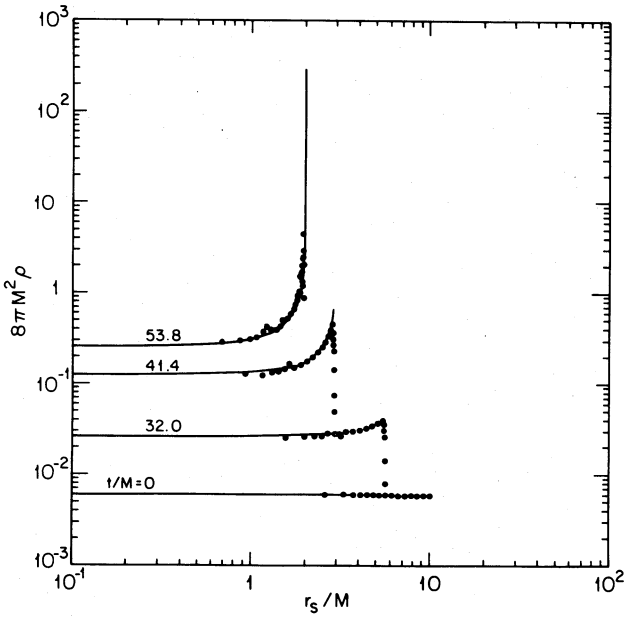

FIG. 6.—Total mass-energy density ρ as measured by a normal observer for the case described in Fig. 3. At $t = 0$ the configuration is homogeneous.

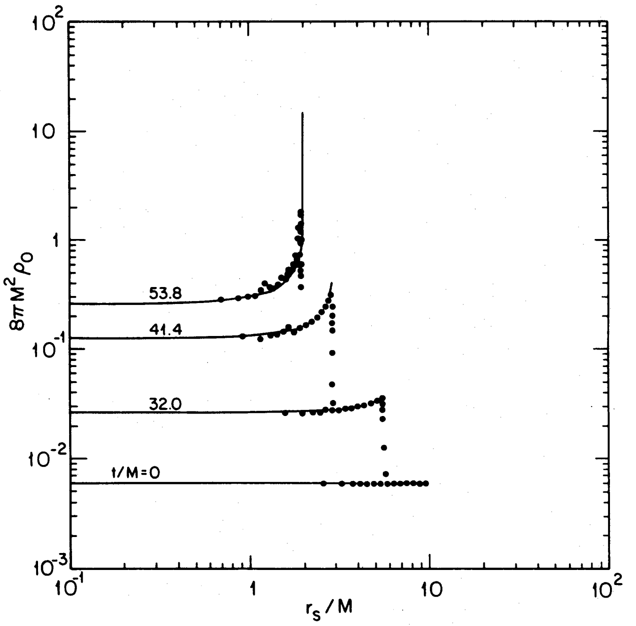

FIG. 7.—Rest-mass density ρ_0 as measured by a normal observer for the case described in Fig. 3. At $t = 0$, $\rho_0 = \rho$.

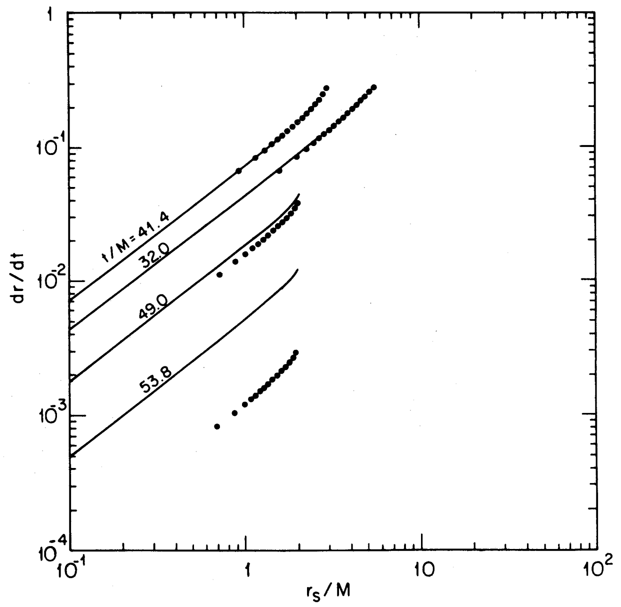

FIG. 8.—Inward radial velocity dr/dt for the case described in Fig. 3. At $t = 0$, $dr/dt = 0$ everywhere.

exactly in spherical symmetry (see § II*a*). The outer boundary can also be placed arbitrarily close to the matter surface in polar slicing, whereas it must be located at a large radius $r_{\max} \gg M$ in maximal slicing to impose the asymptotic boundary conditions accurately. For the case illustrated here we fix $r_{\max}/M = 20$.

The metric profiles are plotted in Figures 3, 4, and 5 on selected polar hypersurfaces labeled by t/M. Solid lines give the exact PST2 values, while filled dots show the corresponding computer generated points. The plot for α in Figure 3 shows good agreement at early times. However, at late times, well after the appearance of an event horizon, the numerical value of the collapsing central lapse function begins to lag somewhere behind the exact value. This lag is due to the sensitive dependence of α on the precise location of the outermost particle, which determines the surface of the dust ball, at late times. According to equation (13), as the matter surface approaches its asymptotic value $r/M = 0.5$ ($r_s/M = 2$), the lapse plunges to

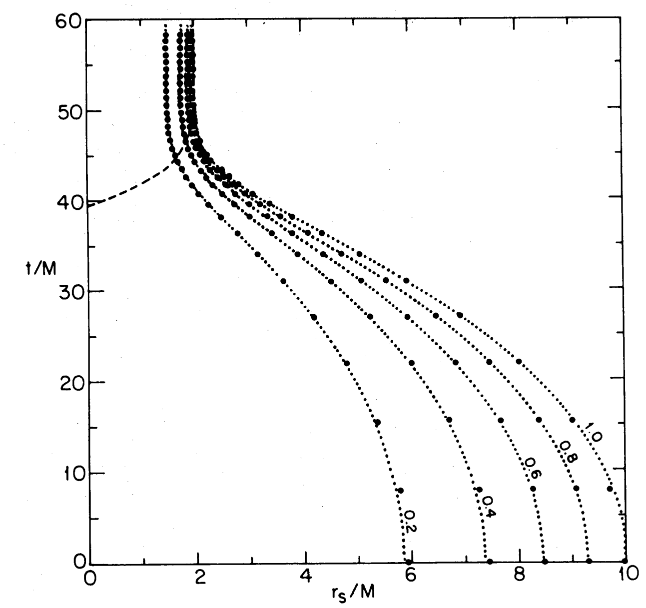

FIG. 9

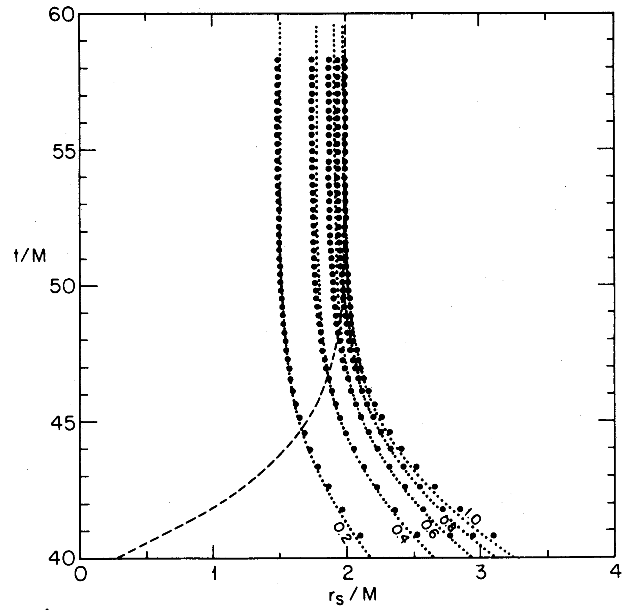

FIG. 10

FIG. 9.—Spacetime diagram for Oppenheimer-Snyder collapse in polar slicing from $R = 10\ M$. Dotted lines are the world lines of Lagrangian matter elements from the exact integrations of PST2. Each world line is labeled by the fixed interior rest-mass fraction. Dots are points for the corresponding matter elements obtained with the hybrid code described in the text. Dashed line is the event horizon.

FIG. 10.—Blowup of Fig. 9 at late times. See text for discussion.

zero there as $1 - M/2r$. Any departure, however small, of the surface particle from its exact asymptotic position $r_{\max} \to 0.5^+$ leads to a large fractional departure in α from its exact value both at the surface and throughout the interior. Since virtually all of the matter is inside the event horizon at $r_H/M \to 0.5^-$ at this point, the effect of such an error on the particle trajectories, which tend to freeze, is practically negligible. This fact is evident from Figures 9 and 10, which we discuss below. Similar discrepancies in the numerical values of the metric coefficients A and β, plotted in Figures 4 and 5, respectively, also occur at sufficiently late times that the matter trajectories are unaffected.

Corresponding matter profiles on selected time slices are plotted in Figures 6–8. The slight lag of the outermost particles at late times is again responsible for the partial failure of the densities to climb sufficiently rapidly at the surface. In the exact solution the plotted densities become infinitely steep at the surface as $t \to \infty$. It becomes increasingly difficult to realize such a steep rise in any simulation code with only a finite number of particles.

Perhaps the most revealing figures are the spacetime diagrams shown in Figures 9 and 10, where the world lines of Lagrangian matter tracers are plotted. Figure 10 zooms in on the region near the center at late times to analyze the formation and growth of the central black hole. The smooth dotted lines show the exact trajectories, while the heavy dots give the computer-generated values. The dashed line shows the event horizon found from the exact solution.

The matter world lines are evidently well reproduced by the hybrid code at all times during the collapse. The steep vertical slope of the world lines at late times confirms that the areal radii of the dust particles tend to freeze. We know that if the matter surface collapsed inside the event horizon a trapped surface would appear, as in the usual exterior Schwarzschild solution. It is thus expected that in the polar gauge, where trapped surfaces are not allowed (see § II*a*), the matter surface can approach, but never cross into, areal radius $r_S/M = 2$. This expectation is rather accurately realized in the numerical simulation, as is seen from the figure. However, tiny numerical inaccuracies here are responsible for larger errors in the metric coefficients at late times, as discussed above. Nevertheless, the event horizon trajectory as determined numerically by sending out pairs of outgoing radial light rays (see Paper I) is in excellent agreement with the exact trajectory plotted in Figures 9 and 10. In addition, no trapped surfaces show up in the numerical data.

Comparison of Figures 8 and 9 in Paper I with Figures 9 and 10 here shows how in the case of homogeneous dust collapse polar slicing is more successful in holding back the collapse than maximal slicing. In maximal slicing the matter surface approaches a much smaller "limit surface" near $r_S/M = 1.5$ at late times, and a trapped surface appears. This is in significant contrast to the polar slicing solution summarized here. Our numerical studies of other examples indicates that this contrasting behavior is typical of more general spacetimes and is not peculiar to dust collapse.

The polar slicing solution found with the other versions of our numerical code is quite comparable in accuracy with the hybrid version shown here for a comparable set of input integration parameters. Accordingly we omit further details.

IV. NUMERICAL EXAMPLES

In this section we demonstrate the power of our numerical method by examining some concrete examples. We focus on several of the isotropic, unstable equilibrium configurations whose evolution was already considered in a preliminary manner in Paper II. Our ability to overcome some of the limitations inherent in our original treatment will become apparent.

a) Truncated Maxwell-Boltzmann Distributions

We reconsider the catastrophic collapse of an unstable equilibrium cluster constructed from the truncated Maxwell-Bolzmann isothermal distribution function given in equation (II.4). In Paper II considerable attention was focused on model b of Figure 2 (see § II*a*, and especially Fig. 3 of that paper), and it is this case that we reanalyze now. The cluster has central redshift $z_c = 0.517$, areal radius $R/M = 9.16$, and mean-to-central total mass-energy density ratio $\langle \rho \rangle / \rho_c = 7.8 \times 10^{-2}$. Thus this cluster is neither very centrally condensed, nor does it have a substantial Newtonian halo. We utilize the standard code in both maximal and polar time slicing to study the collapse of this unstable configuration to a black hole.

The geometry of the collapse is shown in the spacetime diagram plotted in Figure 11 for maximal time slicing and in Figure 12 for polar time slicing. Both figures show the late time behavior beginning when the black hole first appears at the center and then following its monotonic outward growth. The world lines of imaginary Lagrangian matter tracers in the cluster, the black hole event horizon, and, in the case of maximal slicing, the region of trapped surfaces are shown.

The key difference between the new maximal computation summarized in Figure 11 and the old one summarized in Figure 3 of Paper II is the use of the revised time-step criterion equation (37) in the new version instead of equation (I.62). The revised criterion permits us to follow the evolution much further in time: the original calculation terminated when $t/M = 272$, after which further integration became very slow and

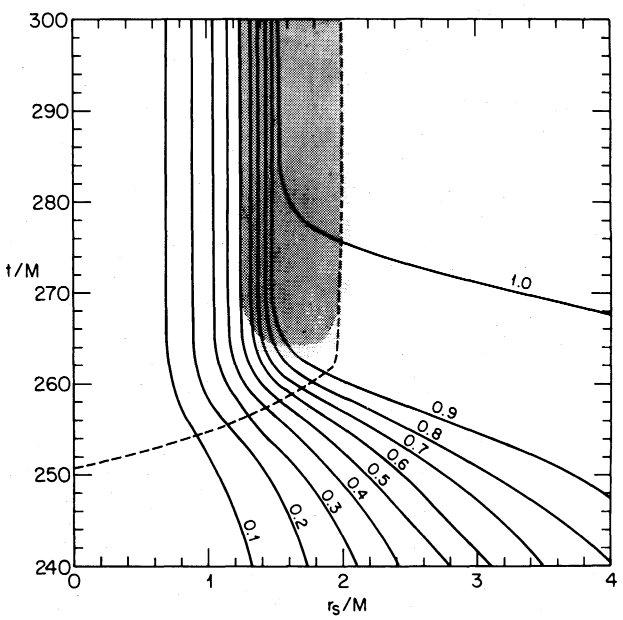

FIG. 11.—Spacetime diagram in *maximal* slicing for the Maxwell-Boltzmann cluster originally plotted in Fig. 3 of Paper II. Dotted lines are the world lines of fictitious Lagrangian matter tracers labeled by the fixed interior rest-mass fraction. Dashed line is the event horizon, determined by pairs of light rays emitted from the same radius at different times. Shaded area is the region of trapped surfaces. The event horizon and apparent horizon both numerically asymptote to $r_S = 2\ M$ to high accuracy.

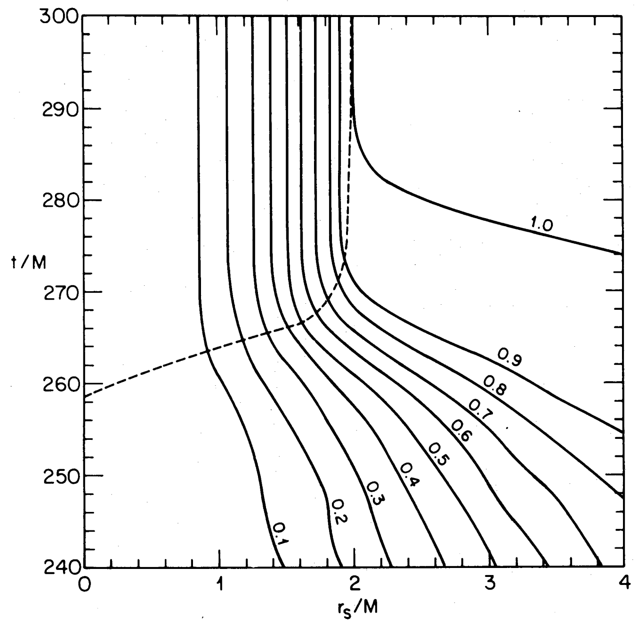

FIG. 12.—Spacetime diagram in *polar* slicing for the Maxwell-Boltzmann cluster considered in Fig. 11. No trapped surface forms in polar slicing. The event horizon and matter surface both numerically asymptote to $r_S = 2\ M$ to high accuracy.

inefficient, while the present calculation terminates when $t/M = 340$ and could be continued considerably longer without encountering numerical difficulties. In maximal time slicing, the central lapse function falls only to $\alpha_c = 4.8 \times 10^{-4}$ by $t/M = 272$ but subsequently plummets to $\alpha_c = 7.3 \times 10^{-20}$ by $t/M = 340$. While the evolution is almost complete by $t/M = 272$ (virtually 99.9% of the rest mass lies inside the event horizon at this point), determining the complete evolution, including the location of the inner horizon and limit surface, requires the longer integration shown in Figure 11.

In polar slicing the collapsing surface asymptotes to radius $r_S/M = 2$ as in the case of homogeneous dust collapse. To collapse further would result in the formation of a trapped surface, which cannot happen in this time gauge. In maximal slicing the surface asymptotes to $r_S/M \approx 1.5$, well inside the event horizon at $r_S/M = 2$, and a trapped surface does form. These differences are all evident from Figures 11 and 12. They are also evident from Figure 13, which compares snapshots of the central region of the cluster at early and late times during the collapse in the two time slicings.

Finally we note that at late times the Lagrangian matter world lines are vertical, as the particle areal radii freeze. This behavior is expected (see eq. [30]) and motivates the other two versions of the code based on freezing.

b) Relativistic Polytropes with $n = 4$: Extreme Core-Halo Configurations

Relativistic polytropes with index $n = 4$ and $\Gamma = 5/4$ provide a convenient sequence of equilibrium models characterized by extreme core-halo distributions (i.e., strong central concentration). Fackerell (1970) has shown that their phase space distribution function is given by the exact equation (II.9) with $\delta = 5/2$. He studied the equilibrium and stability properties of these models extensively in perturbation theory. Our standard code was employed in Paper II to locate the point of dynamical instability accurately along the equilibrium sequence and to explore the full nonlinear evolution of unstable models. The extreme core-halo configurations along the unstable branch of the $n = 4$ sequence, and the black holes to which they give birth, provide a useful proving ground for testing the ultimate capabilities of our code, particularly the freezing version. This realization, together with the potential astrophysical importance of such extreme core configurations (see Paper III and § V below), motivates our reanalysis of these polytropic models in this section.

We shall focus on the evolution of the unstable configuration located just beyond the first fractional binding-energy maximum in the equilibrium sequence plotted in Figure 11 of Paper II. This model has a highly relativistic core with central redshift $z_c = 0.50$ and a substantial Newtonian halo, extending out to radius $R/M = 5.2 \times 10^3$. The rest-mass density profile is plotted in Figure 14, and the density contrast is $\langle \rho \rangle / \rho_c = 4.0 \times 10^{-13}$. The central core, i.e. the region within which the rest-mass density falls by no more than one-half of its central value, is quite small: it is confined to the domain $0 \leq r_S/M \leq 7.7 \times 10^{-2}$ and contains only 0.48% of the total rest mass.

The standard code was employed in Paper II to follow the catastrophic collapse of this marginally unstable, extreme core-

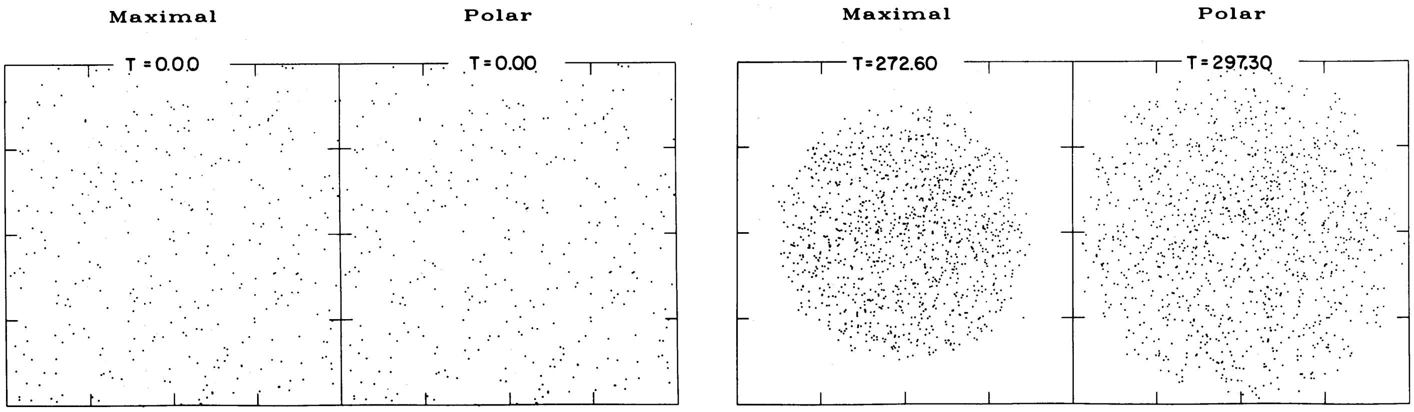

FIG. 13*a* FIG. 13*b*

FIG. 13.—Snapshots of the central regions of the Maxwell-Boltzmann cluster of Figs. 11 and 12. (*a*) The initial configuration is plotted, which is identical in both time slicings. (*b*) The configuration at a late time (in units of M) is shown in both slicings. Spatial grid markers correspond to 1 M in areal radius r_S. In maximal slicing the surface approaches an asymptotic limit near $r_S/M = 1.5$. In polar slicing the surface asymptotes to $r_S/M = 2$.

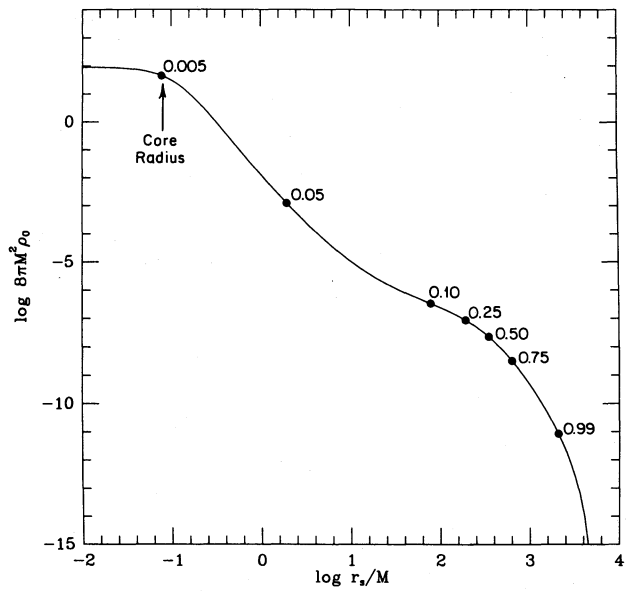

FIG. 14.—Initial rest-mass density profile ρ_0 for the relativistic polytrope with $n = 4$, $\Gamma = 5/4$, and central redshift $z_c = 0.50$. Dots are located at points at which the interior rest-mass fraction has the values shown. This is an extreme core-halo configuration, with a highly relativistic core and an extensive Newtonian halo. At the end of the evolution calculation the black hole contains a fraction 0.05 of the total rest mass, ~ 10 times the initial core mass.

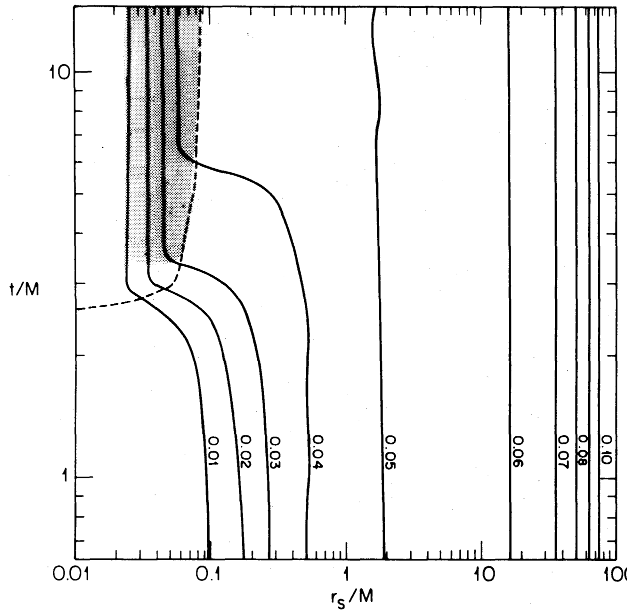

FIG. 15.—Spacetime diagram in *maximal* slicing for the relativistic polytrope described in Fig. 14. Solid lines are the world lines of imaginary Lagrangian matter tracers labeled by their fixed interior rest-mass fraction. Dashed line is the event horizon, and shaded area is the region of trapped surfaces. The event horizon is still growing when the calculation is forced to terminate.

halo configuration. Maximal time slicing was used, together with the original time-step criterion equation (I.62). By $t/M = 5.4$ further integration became inefficient, and the calculation was terminated. However, already by that time a full 3.1% of the total rest mass had formed a central black hole. Unfortunately, the final fate of the cluster, including the final mass of the black hole, could not be determined by this preliminary calculation.

We have reanalyzed the collapse of this model numerically using several of the new options now available to us. We have rerun our standard code again but now using the new time-step criterion equation (37). The calculation was performed in both maximal and polar slicing. To achieve the required dynamic range to accurately evolve this cluster, we employed $N_f = 3800$ radial grid points to compute the metric field quantities. Of these, 3600 were used to cover the matter interior, with the rest residing in the vacuum exterior. The total number of particles tracked was $N_p = 7198$, and the nondimensional time-step parameter q appearing in equation (37) was set at 0.05.

The resulting maximal spacetime is summarized in Figures 15–17. This time the integration continued smoothly until $t/M = 14.4$, at which point $\alpha_c = 9.2 \times 10^{-70}$ and $A_c = 1.5 \times 10^{49}$ (sic!). Soon after this time the integration was forced to terminate because of computer overflows associated with the huge value of the conformal factor, A, near the center of the cluster. Note that cutting α off at some value $\alpha_{\min} \ll 1$ would not circumvent this problem. Since the black hole is still growing and the ambient cluster has not yet reached a stationary equilibrium about the hole when the overflow occurs (see Fig. 15), we conclude that *maximal time slicing and isotropic coordinates is not a good gauge in which to solve this problem.* At $t/M = 14.4$, a full 4.4% of the total cluster rest mass has fallen into the central hole. This represents over 9 times the initial core mass and strengthens the claim in Paper II that *even in the case of extremely condensed configurations with extensive Newtonian halos, an appreciable fraction of the total cluster mass collapses to a central black hole in a few dynamical times, provided the central redshift is sufficiently relativistic.* Nevertheless, *the complete dynamical evolution cannot be determined by a calculation in these coordinates.*

Repeating the calculation in polar time slicing did not prove significantly better when our standard code was employed.

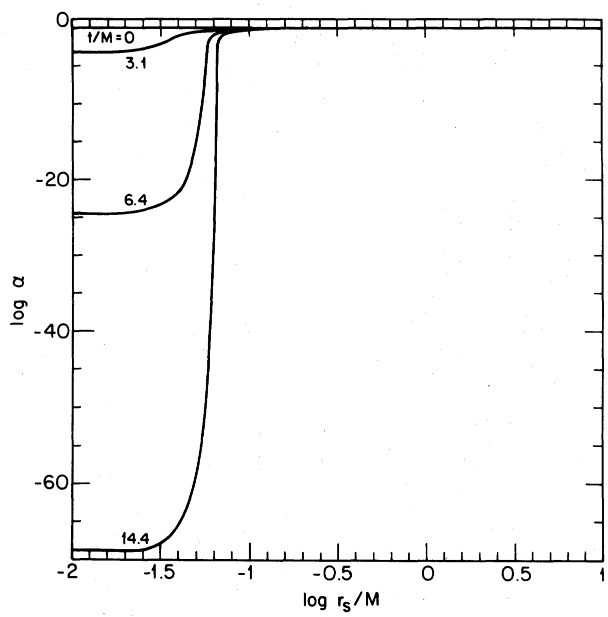

FIG. 16.—Lapse function α as a function of areal radius r_S on selected maximal time slices for the cluster shown in Fig. 15.

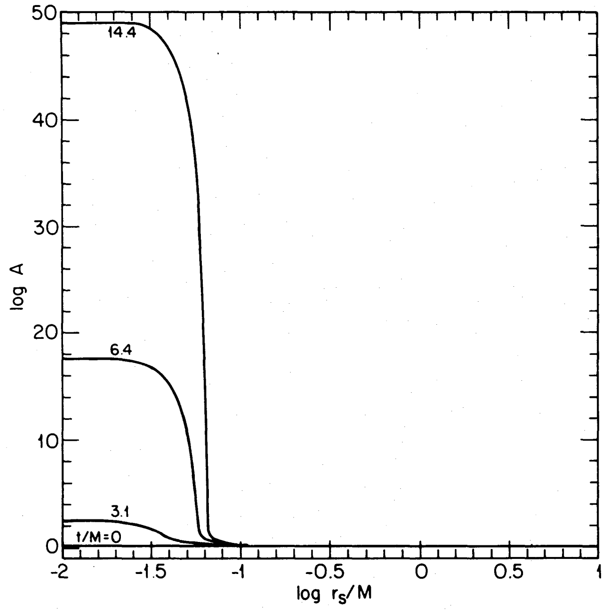

FIG. 17

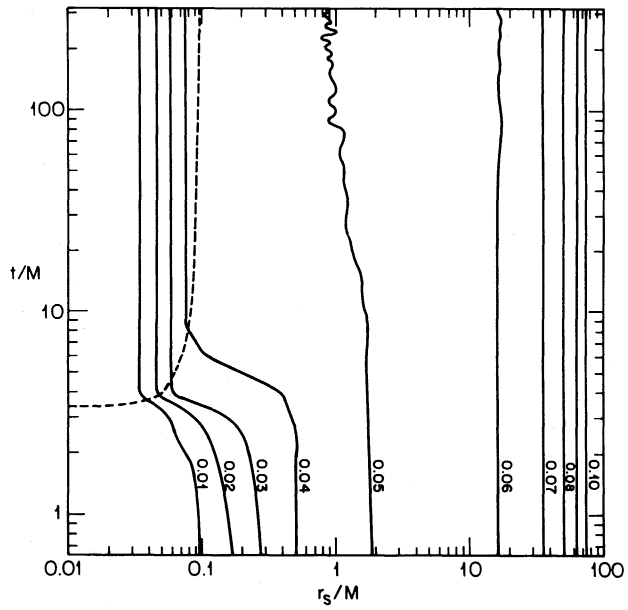

FIG. 18

Fig. 17.—Metric component A as a function of areal radius r_S for the case described in Fig. 16.

FIG. 18.—Spacetime diagram in *polar* slicing for the relativistic polytrope described in Fig. 14. Solid lines are the world lines of imaginary Lagrangian matter tracers labeled by their fixed interior rest-mass fraction. Dashed line is the event horizon. The event horizon asymptotes to $r_S/M = 0.1$, at which point it encompasses 4.9% of the total cluster rest mass.

Although the central conformal factor A_c does not grow nearly so rapidly with time in polar slicing, *grid stretching along the black hole throat becomes a severe problem in isotropic coordinates*, causing the calculation to lose accuracy by the time 4.0% of the rest mass is inside the event horizon. Increasing the number of radial grid points by a factor of 2 does not improve the situation noticeably.

Only by utilizing the freezing version of our code, which is also based on polar slicing and an isotropic spatial line element but uses r_S instead of r to eliminate grid stretching, are we able to determine the final fate of this cluster successfully. The adopted integration parameters for this case were identical to those chosen for use in the standard code (see above). The resulting spacetime is plotted in Figure 18, and the corresponding metric profiles in Figures 19 and 20. The integration is continued until $t/M = 439$, when it is halted because by this time the black hole mass has ceased growing appreciably and the cluster has essentially settled into a new dynamical equilibrium about the central hole (see Fig. 18). Thus *the freezing version is able to follow the catastrophic collapse of an extreme core-halo configuration to completion.* This calculation took ~ 10 CPU hours on an FPS 164 Array Processor. Were the integrations not terminated the code would clearly continue to integrate reliably for a considerably longer time, since A_c does not increase very rapidly in polar slicing (see Fig. 20). (Note that to prevent possible underflows at late times, the lapse function α was never allowed to fall below 10^{-15}, as is evident from Fig. 19. This numerical fix has no influence on the dynamical evolution, since the particle orbits freeze for all $\alpha \ll 1$; see eq. [30].)

The final black hole contains 4.9% of the cluster rest mass. This is more than 10 times the initial central core mass. This value is consistent with the final location of the event horizon at areal radius $r_H/M = 0.1$, i.e. $r_H/M_H \approx 2$. As a check, we carried out a longer run, setting $q = 0.1$ in equation (37). This run reached $t/M = 1030$, at which point the black hole mass had not increased from the value of 4.9%.

Snapshots of the central regions of the cluster inside $r_S/M = 100$ are shown in Figure 21 at selected early and late times during the collapse. Blowups of these snapshots which zoom into the innermost regions inside $r_S/M = 2$ are shown in Figure 22. It is evident from these figures and from corre-

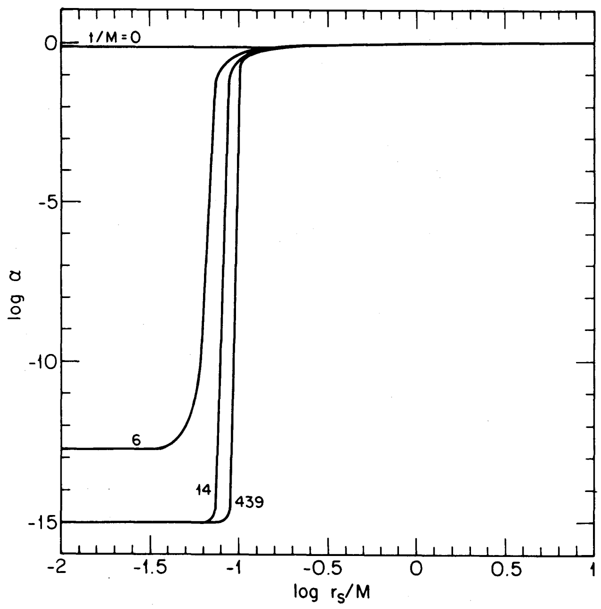

FIG. 19.—Lapse function α as a function of areal radius r_S on selected polar time slices for the cluster shown in Fig. 18. The quantity α is cut off at a minimum value of 10^{-15} in the numerical calculations. See text.

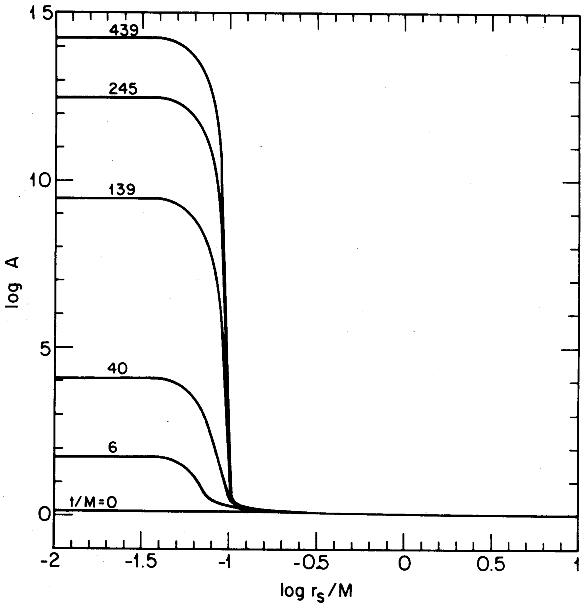

FIG. 20.—Metric component A as a function of areal radius r_S for the case described in Fig. 18.

sponding density plots that the cluster profile does not evolve measurably in the outer Newtonian halo where most of the mass originates. However, the black hole is effective in "sweeping clean" the innermost regions in and around the core. It is also clear from Figure 22 that the cluster does not evolve much after $t/M = 40$ except for the steady orbiting of ambient stars about the central hole.

The orbital trajectories of four typical particles near the cluster center are plotted in Figure 23. Interior to particle N at $t/M = 0$ resides a fraction $N/N_p = N/7198$ of the total cluster rest mass. Particle 333, which is initially in an elliptical-like orbit near $r_S/M = 1$, experiences inward spiral motion leading to capture by the black hole after two orbital periods. Particle 410 falls nearly radially from $\sim 7M$ into the black hole. Particle 340 moves nearly unperturbed in a circular orbit at $1M$. Particle 338 moves in a nearly elliptical orbit extending out to $1.5M$ which exhibits large perihelion precession about the central hole but is never captured. Pericenter for this orbit appears to be one of the closest of all the ambient particles which do not get captured. It is located at $r_S/M = 0.25$ or $r_S/M_H \approx 5$. This is consistent with the fact that particles which orbit a stationary Schwarzschild black hole inside $r_S/M = 4$ are inevitably captured (see, e.g., Misner, Thorne, and Wheeler 1973). It is also satisfying that the pericenter position of this marginally stable orbit remains stationary with time, further confirming that *by the time our integrations terminate, the cluster has achieved a new dynamic equilibrium about a stationary central black hole.*

V. DISCUSSION

a) *Astrophysical Implications*

There is strong evidence that quasars, AGNs, and other intense extragalactic radio sources are powered by magnetohydrodynamic jets and that each jet is produced by a compact

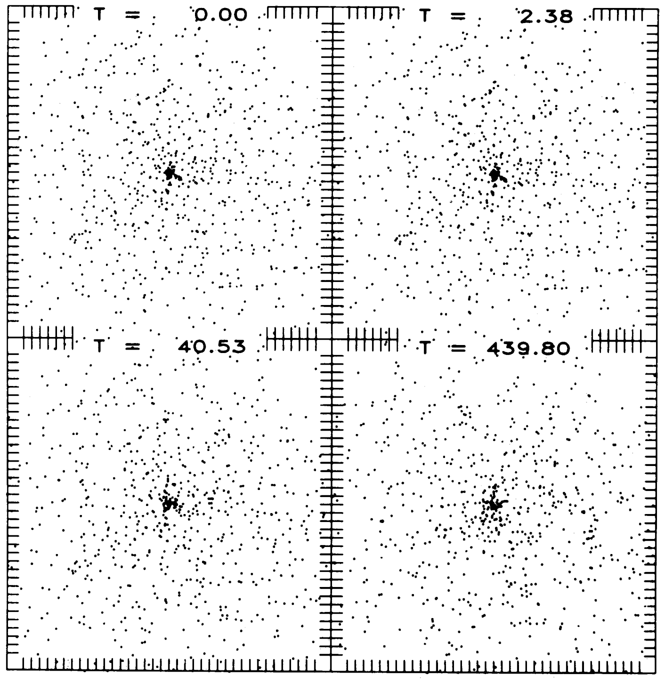

FIG. 21

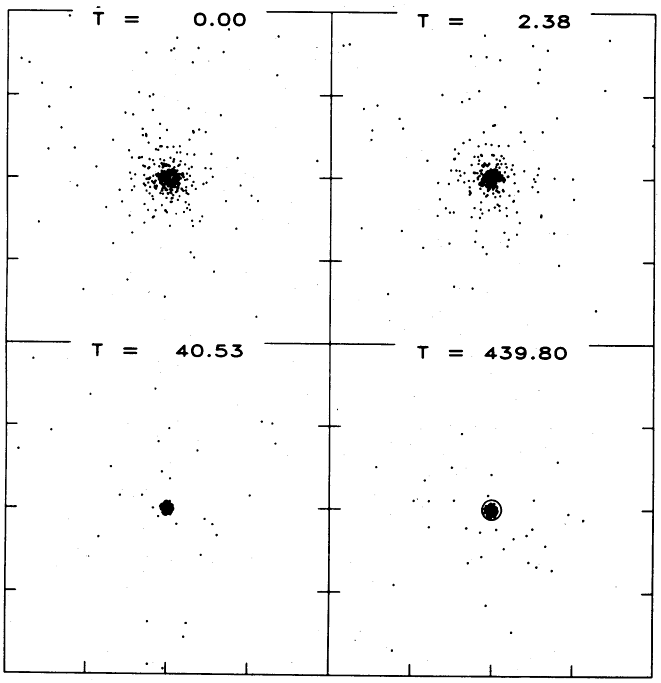

FIG. 22

FIG. 21.—Snapshots of the central regions $r_S/M \leq 100$ of the extreme core-halo configuration shown in Fig. 18. Interval between radial grid markers is $\Delta r_S = 5\ M$. Pictures are at selected early and late times (in units of M) during the collapse. The formation of the central black hole does not measurably affect the Newtonian halo, even in the region $r_S/M \lesssim 100$ shown here.

FIG. 22.—Blowups of the snapshots shown in Fig. 21, zooming in to the region $r_S/M \leq 2$. The interval between radial grid markers is $\Delta r_S = 1\ M$. Here the collapse of the innermost regions to a black hole is evident. Circle in the last frame shows the event horizon at $r_S/M = 0.1$. Note that the cluster does not evolve appreciably after $t/M = 40$, but is characterized by the steady orbiting of stars about the central black hole.

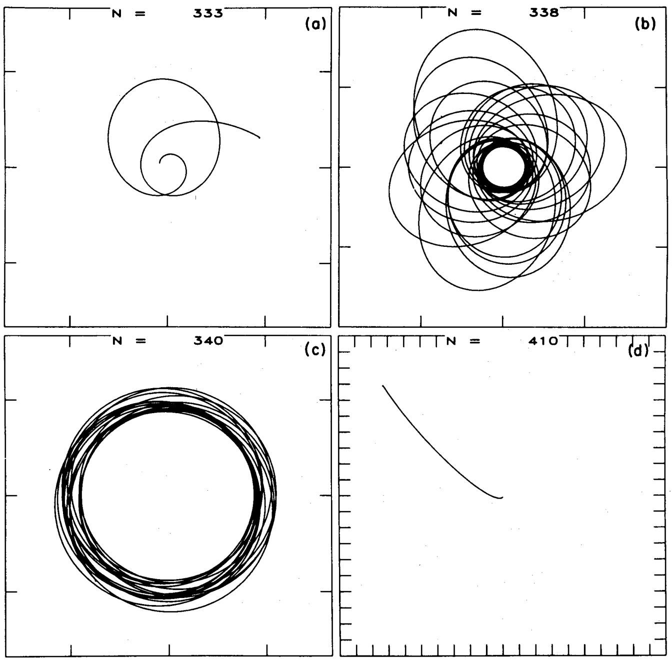

FIG. 23.—Orbital trajectories of four typical particles near the cluster center. Each particle N surrounds a fraction $N/7198$ of the total cluster rest mass at $t = 0$. In each frame the spacing between radial grid marks is $\Delta r_S = 1$ M. (a) The particle is initially in an elliptical-like orbit, but spirals in to the black hole after roughly two orbits. (b) The particle moves in a nearly elliptical orbit, exhibiting large perihelion precession about the central black hole. Pericenter for this particle, $r_S/M = 0.25$, is one of the closest of all the particles that do not get captured, and remains stationary in time. (c) The particle moves essentially unperturbed in a nearly circular orbit. (d) The particle falls nearly radially into the black hole.

supermassive object $M \gtrsim 10^6$–10^9 $M_\odot$. A supermassive black hole is the likely candidate for the compact object (see reviews by Begelman, Blandford, and Rees 1984; Rees 1984, and references therein). The dynamical evolution of a dense stellar system containing a central supermassive black hole has been extensively studied (Hills 1975; Rees 1978; Young, Shields, and Wheeler 1977; Frank 1978; McMillan, Lightman, and Cohn 1981; Duncan and Shapiro 1983). Gas expelled during star-star collisions and tidal disruptions by the hole is consumed by the hole, causing it to grow significantly. This gas accretion, leading to radiation near the Eddington limit, provides an efficient means by which black holes in the above mass range can generate the underlying power observed from quasars and AGNs.

In Paper III we addressed the question: *how and under what circumstances did such a supermassive black hole form*? We explored a plausible scenario by which a dense cluster of compact stars—neutron stars or stellar-mass black holes—embedded in a galactic nucleus can evolve via the "gravothermal catastrophe" to a relativistically unstable state in a Hubble time and subsequently undergo catastrophic collapse to a supermassive black hole (see Zel'dovich and Podurets 1965). Immediately prior to collapse, the cluster is extremely centrally condensed with a highly relativistic core and extensive Newtonian halo. We showed that the collapse leads naturally to the formation of black holes of the "right size" to explain quasars and AGNs: $10^6 \lesssim M/M_\odot \lesssim 10^9$.

Crucial to the viability of the above scenario are the requirements that an unstable relativistic star cluster with an extensive Newtonian halo (1) collapse to form a black hole at the cluster center in a few mean dynamical (orbit) time scales; (2) produce a hole containing a nonneglible fraction of the total cluster mass (i.e., many times the mass of the small central core) with the bulk of the cluster stars remaining outside in orbit about the hole; and (3) settle down to a new, dynamically stable, equilibrium state consisting of a massive, central black hole embedded in a quasi-Newtonian star cluster. In this paper we have rigorously demonstrated that the catastrophic collapse of an extreme core-halo cluster meets these requirements. Hence, *our numerical computations point to a possible route by which supermassive black holes can form in nature and lend credibility to the suggestion that quasars and AGNs are actually born by this process.*

As discussed in Paper II, the fact that a nonnegligible fraction of the total cluster mass can collapse to a black hole in a few crossing time scales is due to a collective dynamical instability predicted by Zel'dovich and Podurets (1965) and termed "avalanche-type contraction" by them. Essentially, stars outside the unstable relativistic core, which readily collapses, feel an ever increasing interior mass with time. This increase is due to inward moving stars from the halo on radial trajectories which are quickly captured by the nascent hole and never return to the halo. Hence, stars initially outside the core on only mildly eccentric orbits have an increasing probability of being captured as they are pulled ever closer to the *growing* hole at the center. The growth runs away, and a cascade ensues. An appreciable mass, whose actual size depends on the precise stellar distribution function outside the core at the onset of collapse, is thus able to form a black hole in a few orbital periods. This mass may be many times the mass of the central core, as we have demonstrated.

The orbit plotted in Figure 23a illustrates the avalanche instability at work. For almost two orbits the particle moves in an elliptical-like trajectory, essentially unaffected by the catastrophic collapse taking place at the cluster center. Eventually, the mass interior to this particle at pericenter grows sufficiently that the particle now finds itself on a capture orbit and spirals in to the black hole.

It is not possible to predict the mass of the final black hole without a detailed numerical calculation such as we have performed. However, one can crudely estimate an *upper* limit to the fraction of stars F that can form a black hole following the collapse of an unstable, isotropic, spherical cluster in which most of the mass resides in a Newtonian halo.

The critical specific angular momentum for the capture of a nonrelativistic particle by a massive Schwarzschild black hole is $4M_H$, where M_H is the hole mass. The critical tangential velocity for the capture of such a particle orbiting at areal radius r_S is then $v_c^\phi = 4M_H/r_S$ as measured by a local orthonormal observer. Thus the fraction ΔF of all stars within Δr_S of r_S which is captured is

$$\Delta F = 2 \times \frac{1}{4\pi} \times \int_0^{2\pi} \int_{\cos\theta_c}^{1} d\phi \, d\cos\theta \,, \tag{38}$$

where

$$\sin\theta_c = \frac{v_c^\phi}{v_m} \tag{39}$$

defines the critical angle for capture, v_m is a suitable mean velocity at r_S, and the factor of 2 appearing in equation (38) accounts for the ultimate capture of both ingoing *and* outgoing particles moving in the critical solid angle. Since $\sin\theta_c \ll 1$ in the Newtonian halo, we have

$$\Delta F \approx \frac{1}{2}\left(\frac{v_c^\phi}{v_m}\right)^2 \approx 8\left(\frac{M_H}{r_S v_m}\right)^2 . \quad (40)$$

(Eq. [40] shows that the appropriate definition of v_m is that v_m^{-2} is the mean inverse square velocity at r_S.) Multiplying by $\Delta N/N$, the fraction of all stars in the cluster within Δr_S of r_S, and integrating over all r_S yields F, the fraction of all cluster stars which are captured by the central hole.

We can crudely approximate this integral by evaluating equation (40) at, say, the cluster half-mass radius R_h, where we can set $v_m^2 \approx M/R_h$. However, we do not know *a priori* what value to insert for the final black hole mass. We can get an *upper* limit to F by setting, in zeroth order, M_H equal to the total cluster mass M in equation (40). This yields a first-order estimate for the upper limit,

$$F \lesssim 8\left(\frac{M}{R_h}\right) . \quad (41)$$

This estimate is clearly quite rough, and the numerical factor appearing in equation (41) is very uncertain. Moreover, the scaling does not adequately account for the details of the cluster profile. However, we have found empirically that equation (41) does give a reasonable estimate, not just an upper limit, for the final black hole mass. For the marginally unstable $n = 4$ polytrope discussed in § IV, we have $R_h/M = 354$, for which equation (41) gives $F \approx 0.023$. To within a factor of 2 this answer is consistent with the value 0.049 found from our detailed numerical computations. Another case one can compare is a more extreme configuration on the same equilibrium sequence, with $z_c = 0.73$ and $R/M = 7.5 \times 10^3$. This cluster also has an extensive Newtonian halo and a tiny relativistic core containing only 0.6% of the total rest mass. For this cluster $R_h/M = 89$ and $F = 0.09$ according to equation (41). This compares with the numerical value of 0.08 from the simulation, or almost 13 times the core mass. A third comparison is given by noncentrally condensed clusters with relativistic cores, like the Maxwell-Boltzmann cluster with $R/M \approx 9$ discussed in § IV*a*. Such clusters undergo *total* gravitational collapse, in agreement with the estimate $F \approx 1$ from equation (41).

In Paper III we argued that a cluster of compact stars capable of evolving to a relativistically unstable state within a Hubble time would typically have a mass $M \approx 10^9\ M_\odot$ and a radius $R_h \approx 0.1$ p.c. Equation (41) then gives $F \approx 10^{-3}$, so that the typical black hole would form with a mass $\approx 10^6\ M_\odot$. Even if equation (41) greatly overestimates the mass, the resulting supermassive black hole is still likely to be substantial. If it is only 10 $M_{\rm core}$, as in the case discussed in § IV, then the black hole will still be $\approx 1000\ M_\odot$. This is a substantial seed mass that can grow by accretion following physical collisions and tidal disruptions of stars.

Any anisotropy characterized by preferential *radial* motion in the velocity distribution of the halo stars prior to collapse would result in a larger black hole mass. Such an anisotropy is inevitably induced by two-body gravitational encounters which drive the gravothermal catastrophe (see Spitzer and Shapiro 1972 or Lightman and Shapiro 1978). On the other hand, the presence of rotation in the cluster, apart from generating a burst of gravitational radiation during the implosion, might inhibit the formation of a black hole. Unfortunately, determining the fate of a rotating relativistic cluster must await the construction of a reliable $2 + 1$ dimensional code that simulates the Vlasov equation in full general relativity.

b) Numerical Implications

We have succeeded in developing a reliable method that follows the dynamical evolution of collisionless configurations in general relativity. The method is rugged, and the spacetimes generated on the computer are accurate. Although restricted to spherical symmetry, our computational algorithms and numerical examples teach some general lessons about building spacetimes on the computer. For example, our calculations confirm previous speculations (see Piran 1983, and references therein) that polar time slicing has somewhat stronger singularity avoidance features than maximal time slicing. Accordingly, it is often more desirable to work in the polar gauge for solving certain problems, particularly those for which the dynamical evolution must be followed for a very long time $\Delta t \gg M$ after the appearance of an event horizon to reach a final stationary state.

We have also demonstrated, however, that choosing polar slicing is not always in itself sufficient to guarantee numerical success since the selection of well-behaved spatial coordinates is equally crucial to the reliable and trouble-free integration of Einstein's equations on the computer. For example, the adoption of the radial gauge results in the appearance of spikes in the radial metric coefficient whenever a black hole forms. Similarly, the adoption of the isotropic gauge results in severe grid stretching all along a black hole throat.

To circumvent these difficulties we showed that it is sometimes necessary to find variables in terms of which the matter fields effectively freeze near and inside a black hole at late times. We demonstrated that the *areal* radius r_S was such a coordinate and that the ADM equations in *isotropic* coordinates could be easily rewritten in terms of this coordinate in place of the usual isotropic radius r. We suspect that similar coordinates must be employed in higher $2 + 1$ and $3 + 1$ dimensional codes before really reliable numerical spacetimes involving black holes can be generated. This suspicion is based on the expectation that in order to evolve gravitational wave data accurately out to large radii, integrations must still continue for a long time $\Delta t \gg M$ after an event horizon forms near the center of the grid. This situation is quite analogous to that already encountered here in spherical symmetry when we considered the collapse of extreme core-halo configurations to black holes. Finding appropriate freezing variables was motivated and greatly simplified by elementary geometric considerations in the spherical case. Discovering analogous variables in more general, nonspherical cases may prove to be more difficult.

Finally, our experience to date in spherical symmetry suggests that working with the *collisionless* fluid equations in general relativity by a mean-field particle simulation scheme should provide new insights for doing numerical relativity accurately in more complicated, multidimensional cases.

This work has been supported in part by National Science Foundation grants AST 84-15162 and PHY 83-05288 at Cornell University. Computations supporting the research were performed on the Cornell Production Supercomputer Facility which is supported in part by the National Science Foundation and IBM corporation.

APPENDIX A

MEASUREMENT OF THE PARTICLE VELOCITY DISTRIBUTION

An important diagnostic for a star cluster is the velocity distribution of the stars. A procedure for determining this distribution in a numerical simulation was outlined in § III*e* of Paper I, equations (I.54)–(I.61). The procedure requires one to specify the *mean rest frame* of the stars at every point. There is no unique way to do this, and in Paper I we simply averaged the radial 4-velocities of all N_A particles in a given spatial zone:

$$U^r = \frac{1}{N_A} \sum_A u_A^r \, . \tag{A1}$$

We then determined U^0 by the condition $\boldsymbol{U} \cdot \boldsymbol{U} = -1$. Using the metric (1), we thus get

$$U^0 = \frac{A^2 \beta U^r + [(\alpha A U^r)^2 + \alpha^2 - A^2 \beta^2]^{1/2}}{\alpha^2 - A^2 \beta^2} \, . \tag{A2}$$

We call such a rest frame the rest frame of a "comoving observer," because

$$\langle u^r \rangle \equiv \sum_A (u_A^r - U^r)/N_A = 0 \, . \tag{A3}$$

The problem with the comoving observer as just defined is that during collapse to form a black hole the quantity $\alpha^2 - A^2\beta^2 = -g_{00}$ can become negative. If U^r is sufficiently small, then the argument of the square root in equation (A2) is negative, and the comoving observer does not exist. This does *not* happen for the case of Oppenheimer-Snyder collapse, where locally all particles move in the same direction (radially) with the same speed. There $U^r = u_A^r$ independent of the label A, and for a *single* particle the argument of the square root is always positive (i.e., $\boldsymbol{U} \cdot \boldsymbol{U} = -1$ always has a solution since the particles are timelike). Only when we form an average where cancellations are possible in equation (A1) can this pathology arise.

An alternative prescription that avoids the problem is to average the *covariant* component of the 4-velocity:

$$U_r = \frac{1}{N_A} \sum_A u_{r,A} \, . \tag{A4}$$

Then $\boldsymbol{U} \cdot \boldsymbol{U} = -1$ gives

$$U^0 = \frac{1}{\alpha} \left(1 + \frac{U_r^2}{A^2}\right)^{1/2} , \tag{A5}$$

and we get U^r from

$$U^r = -\beta U^0 + \frac{U_r}{A^2} \, . \tag{A6}$$

Clearly there is no possibility of square roots of negative numbers with this definition. However, it is usually *not* a "comoving frame":

$$\langle u^r \rangle \equiv \sum_A (u_A^r - U^r)/N_A = -\beta \sum_A (u_A^0 - U^0)/N_A \, , \tag{A7}$$

which is not zero unless all the particles are moving radially and $U_r = u_{r,A}$, independent of the label A.

A third possible choice is the *normal* observer, defined by taking $\boldsymbol{U} = \boldsymbol{n}$, so that

$$U^0 = \frac{1}{\alpha} \, , \qquad U^r = -\frac{\beta}{\alpha} \, , \tag{A8}$$

(see eq. [I.18]). Again this is a nonsingular choice, but it is essentially *never* a "comoving observer" since $\langle u^r \rangle \neq 0$.

Once we have defined the mean rest frame, for example by one of the three choices above, then equations (I.55)–(I.61) can be used to average 3-velocities and dispersions ("temperatures") of the distribution.

APPENDIX B

PROOF THAT *Adr* FREEZES

In § II*b* we needed to show that the quantity Adr freezes as $\alpha \to 0$ at late times. This is true because Adr is a quantity measurable by the normal observer, but it can also be demonstrated formally from the equations of § II. Since we are performing an integral between fixed values of r_S, if we change the variable of integration to r_S we must show that

$$\left.\frac{\partial}{\partial t}\right|_{r_S} A \frac{dr}{dr_S} \to 0 \tag{B1}$$

as $\alpha \rightarrow 0$. By equation (16) we have

$$A \frac{dr}{dr_S} = 1 - \frac{r_S A_{,r_S}}{A} , \tag{B2}$$

and so

$$\left.\frac{\partial}{\partial t}\right|_{r_S} A \frac{dr}{dr_S} = -r_S \frac{\partial}{\partial r_S} \frac{\partial}{\partial t} \ln A = -r_S \frac{\partial}{\partial r_S}\left[\frac{A\beta}{r_S} - \frac{1}{2}\alpha K_T\left(1 - \frac{r_S A_{,r_S}}{A}\right)\right] = -r_S \frac{dr}{dr_S}\frac{\partial}{\partial r}\left[\frac{\beta}{r} - \frac{1}{2}\alpha K_T\left(1 - \frac{r_S A_{,r_S}}{A}\right)\right] . \tag{B3}$$

Using equation (7) we now see that every term in equation (B3) is proportional to α or $\alpha_{,r}$ and hence freezes.

REFERENCES

Bardeen, J. M., and Piran, T. 1983, *Phys. Repts.*, **96**, 205.
Begelman, M. C., Blandford, R. D., and Rees, M. J. 1984, *Rev. Mod. Phys.*, **56**, 255.
Deruelle, N., and Piran, T., eds. 1983, *Gravitational Radiation, Les Houches 1982* (Amsterdam: North Holland).
Duncan, M. J., and Shapiro, S. L. 1983, *Ap. J.*, **268**, 565.
Eardley, D. M. 1982, unpublished.
Fackerell, E. D. 1970, *Ap. J.*, **160**, 859.
Frank, J. 1978, *M.N.R.A.S.*, **184**, 87.
Hills, J. G. 1975, *Nature*, **254**, 295.
Lightman, A. P., and Shapiro, S. L. 1978, *Rev. Mod. Phys.*, **50**, 437.
McMillan, S. L. W., Lightman, A. P., and Cohn, H. 1981, *Ap. J.*, **251**, 436.
Misner, C. W., Thorne, K. S., and Wheeler, J. A. 1973, *Gravitation* (San Francisco: Freeman).
Oppenheimer, J. R., and Snyder, H. 1939, *Phys. Rev.*, **56**, 455.
Petrich, L., Shapiro, S. L., and Teukolsky, S. A. 1985, *Phys. Rev. D*, **31**, 2459 (PST1).
Petrich, L., Shapiro, S. L., and Teukolsky, S. A. 1986, *Phys. Rev. D*, **33**, 2100 (PST2).
Piran, T. 1983, in *Gravitational Radiation, Les Houches 1982*, ed. N. Deruelle and T. Piran (Amsterdam: North Holland), p. 203.
Rees, M. J. 1978, *Phys. Scripta*, **17**, 193.
———. 1984, *Ann. Rev. Astr. Ap.*, **22**, 471.
Shapiro, S. L., and Teukolsky, S. A. 1985*a*, *Ap. J.*, **298**, 34 (Paper I).
———. 1985*b*, *Ap. J.*, **298**, 58 (Paper II).
———. 1985*c*, *Ap. J. (Letters)*, **292**, L41 (Paper III).
Smarr, L., ed. 1979 *Sources of Gravitational Radiation* (Cambridge: Cambridge University Press).
Smarr, L., and York, J. W. 1978, *Phys. Rev. D*, **17**, 1945.
Spitzer, L., and Shapiro, S. L. 1972, *Ap. J.*, **173**, 529.
Young, P. J., Shields, G. A., and Wheeler, J. C. 1977, *Ap. J.*, **212**, 367.
Zel'dovich, Ya. B., and Podurets, M. A. 1965, *Astr. Zh.*, **42**, 963 (English transl., *Soviet Astr.-A.J.*, **9**, 742 [1965]).

S. L. SHAPIRO and S. A. TEUKOLSKY: Space Sciences Building, Cornell University, Ithaca, NY 14853